An accelerometer for spaceborne application with interferometric readout

An accelerometer for spaceborne application with interferometric readout

Marco Pisani* and Massimo Zucco*
Istituto Nazionale di Ricerca Metrologica
INRIM
Torino, Italy
m.pisani@inrim.it, m.zucco@inrim.it

*These authors contributed equally to this work.

***Abstract*—Accelerometers for space applications are typically based on a capacitive readout. Here we present the design of an accelerometer based on a classical mass spring mechanical system with an interferometric readout. The heterodyne interferometer is completely fiber based with a 1064 nm diode laser source and has a subpicometer resolution at 1 Hz. We present and discuss the design and the characterization of the interferometer, the foreseen performances of the whole accelerometer and the characterization strategies of the same.**

Keywords—Laser interferometer, accelerometer

I. INTRODUCTION

Acceleration measurements are needed to various levels of sensitivity for almost all space missions in the fields of fundamental physics, space geodesy, space exploration, as well as on space stations. Acceleration sensors have a “free” (or weakly coupled) test mass inside a cage rigid with the spacecraft, and yield their relative acceleration by reading the relative displacements (linear and angular, if needed) of the test mass with respect to the cage. The accelerations of interest require very low noise readout also at low frequencies. Typically, the displacement measurement is made with a capacitive sensor with a first armature fixed to the cage, the second one being the mass itself, which is made of, or properly coated with metal [1, 2, 3].

Laser interferometers have demonstrated to be able to measure displacements with accuracies to the level of the picometer [4] and their use is foreseen in high-resolution measurement in space [5]. Today's laser sources -such as solid state diode pumped lasers, extended cavity diode lasers or fiber lasers- can be integrated in compact subsystems suitable for space missions. In addition, a plethora of fiber integrated components (mostly coming from telecom industry) allow us to realize compact and robust interferometers which could be used in the next future in place of capacitive sensors.

Laser interferometry readout has two advantages with respect to capacitive readout. In the first place, the laser interferometer output is linear with the gap D between the test mass and the cage, while it is known that capacitive sensors readout can be linearized only for very small changes in D. Secondly the sensitivity of the interferometer readout is independent on the gap D, while in a capacitive sensor it goes as $1/D$, which leads to using narrow gaps and therefore to facing the related noise sources (e.g. the noise due to residual pressure is larger for narrower gaps). Furthermore, if low frequency thermo-mechanical drifts (i.e. “real” drifts) are properly taken care of, there is no increase of noise due to the laser interferometer at low frequencies.

We report on the design of an accelerometer equipped with an interferometric readout expressly planned for scientific missions where very small accelerations have to be accurately measured. The interferometer is based on an all-fiber heterodyne at $\lambda \approx 1064$ nm.

II. THE ACCELEROMETER

The accelerometer we have designed to demonstrate the feasibility of the interferometric readout is based on a simple mass spring assembly taken from an accelerometer realized by IAPS-CNR for the GGG experiment. The dual axes accelerometer, called ISA-GGG, was intended to monitor the environmental seismic vibrations of the laboratory and is described in [6]. The mass and the spring are machined from the same aluminum block. The principle of the accelerometer is based on a test mass m attached to the cage through the spring with stiffness k, cfr Fig 1. The spring is in fact a thin vertical foil, which allows the mass to move horizontally while keeping it constrained in the vertical axis, as represented in Fig. 9. A damping coefficient ζ, however small, is always present.

The equation of motion of the damped spring is a second order linear differential equation with constant coefficients, where $ma(t)$ is the force applied to the test mass m through the acceleration a(t).

$$m\ddot{x} + k\dot{x} + \zeta x = ma(t) \quad [1]$$

The resonant frequency is given by $\omega_o = \sqrt{\frac{k}{m}}$, which in our case is $\omega_o = 18.8$ rad/s, or equivalently $f_0 \approx 3$ Hz. For excitation frequencies below resonance, and for steady state, the displacement x is given by:

$$x = \frac{m}{k}a = \frac{a}{\omega_o^2} \quad [2]$$

The sensitivity S of the accelerometer is given by the ratio x/a giving $S = \frac{x}{a} = \frac{1}{\omega_o^2}$, therefore the sensitivity S is inversely proportional to the spring constant k. This accelerometer ISA-GGG makes use of a pair of electrodes to read the displacement of the mass and a second pair of electrodes to reduce the spring constant k (increasing the sensitivity) and to move the mass for calibration purposes. In our sensor, the electrodes for the capacitive readout are not used and the mass and the cage will be modified to host the mirrors of the interferometer. The sensitivity S of the accelerometer for high frequency, above the resonant frequency, is independent of the accelerometer parameters and depends only on the angular frequency:

$$S(\omega) = \frac{1}{\omega^2} \quad [3]$$

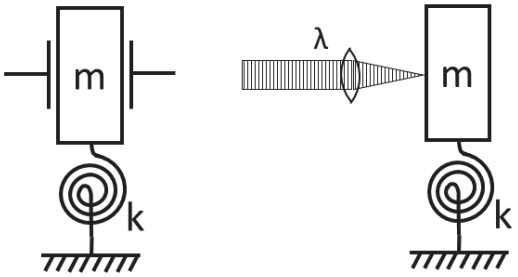

Fig. 1. Left: the classical accelerometer with mass spring assembly and capacitive readout of the displacement. The sensitivity in acceleration is limited by the noise limit of the displacement sensor. Right: the same accelerometer equipped where the displacement of the test mass is measured by an interferometric readout system. The noise of the interferometer can be lower than the capacitive sensor, in particular at large distance between the armatures.

The actuator electrodes will be kept operative for their original purpose, i.e. for in flight calibration and/or for reducing the natural resonant frequency. The same mass spring set-up has been adopted for the three ISA accelerometers of the BepiColombo mission.

III. THE INTERFEROMETER

A schematic diagram of the interferometer readout (here called Laser Interferometry Gauge, LIG) is shown in Fig. 2 where the opto-electronics board contains the readout instrumentation connected through PM fibers to the optical head. The laser source is a continuous-wave high performance Planar-Waveguide External Cavity Diode Laser (PW-ECL) from Redfern Integrated Optics (RIO) working at wavelength λ = 1064 nm. The reason we have chosen this wavelength is because is in coincidence with the emission of Nd:YAG lasers, considered as a standard in the space application since it is used in Lisa pathfinder [7], GRACE Follow-on [8]. The low phase noise of the lasers based on PW-ECL showed that they are good candidates for interferometric applications [9]. Consequently, various opto-electronic and optical components have been space qualified and even used in space. In the scheme, the laser output is directly coupled into a PM fiber and is split into two parts, which undergo differential frequency shifts by means of two acousto-optic modulators (AOM) at frequencies v_2 and v_1. The frequency difference is the heterodyne frequency f_{het}= v_2 - v_1. Then the two radiations are sent through PM fibers to the optical head where a classical polarization separation Michelson interferometer is used to measure the relative displacement between the two mirrors M1 and M2. One of the mirrors will be used as a fixed reference and the other will be fixed to the moving test mass. The mirrors can be indifferently flat mirrors or corner cube retroreflectors (CCR). In our preferred realization, the mirror fixed to the test mass will be a CCR in order to guarantee the self-alignment of the interferometer. The reference signal of the heterodyne interferometer is generated by superposing and making interfere the two radiations spilled from the polarization beam splitter PBS before entering in the interferometer. The interfering beam is sent back through the fiber to the detector on the opto-electronic board. Considering the measurement signal, the second PBS separates the radiations to be sent to the two mirrors M1 and M2 and recombines them in the interfering beam sent to the “measurement” detector on the optical board through the PM fiber. Two half-wave plates at the exit of

the fiber launchers are used to change the power of the beam after the PBS in order to maximize the visibility of the heterodyne signals.

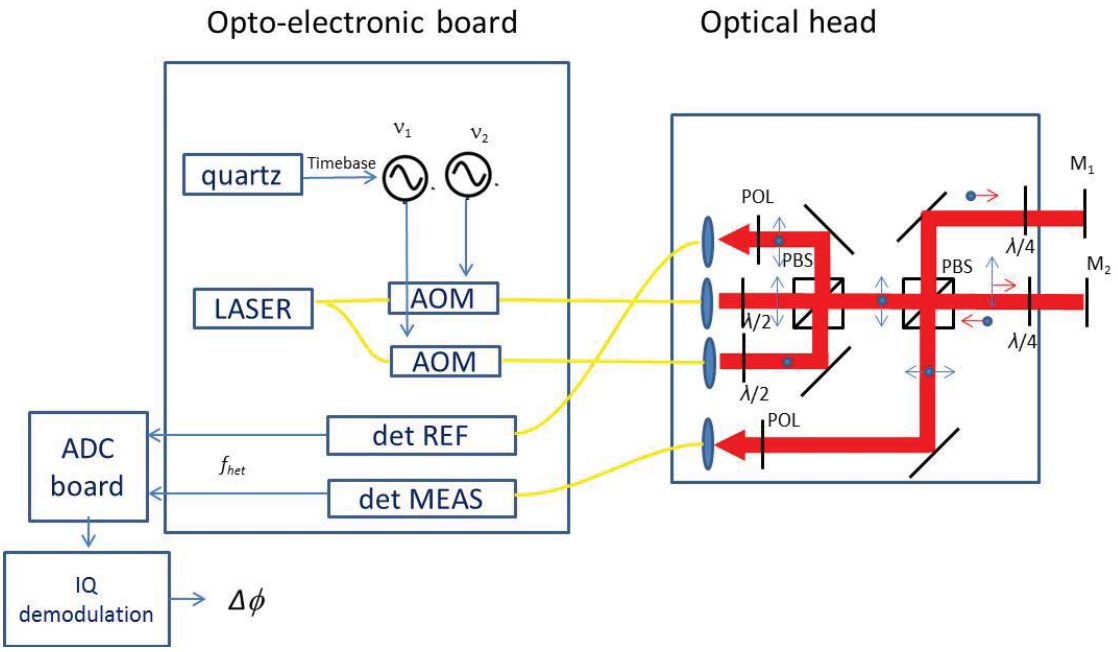

Fig. 2. Schematic of the LIG. The three units are: the opto-electronic board where the instrumentation is present, the optical head with the optical components and the electronics to measure the phase difference. The yellow lines are optical fibers, the red lines the radiations nd the blue lines the electric signals.

In Fig. 3 is shown a picture of the optical part of the LIG prototype. The optical components are glued to a zerodur base. The power of the laser beams reflected on the test masses is kept as low as 1 μW in order to have a negligible effect due to the radiation pressure on the displacement of the masses and a negligible heating of the mass. This power level, on the other hand, is high enough to guarantee a signal to noise ratio, SNR > 10^6 in the band of 1 Hz, to the interferometric signal allowing a resolution better than 1 pm/$\sqrt{\text{Hz}}$ on the displacement PSD.

The two electric signals at f_{het} coming from the two detectors are sent to an A/D converter and elaborated via a LabView® software that implements the IQ demodulation and calculates the phase $\Delta\phi$ between the two signals, hence the relative displacement between the two test masses. The heterodyne frequency could span from few kHz to several hundreds of kHz. We have tested different techniques to measure the phase: time interval counters; XOR logic gates; double balanced mixers and we have found that the IQ demodulation gives the best compromise in terms of resolution and complexity [10].

In the final set-up the interferometer will be built in a quasi-monolithic layout with all the components used in the set-up of Fig. 3 glued into a single block. The final optical assembly will be contained in a 5×5×3 cm^3 volume. Mirror M1 will be fixed to the cage of the accelerometer, while mirror M2 will be fixed to the mass of the accelerometer. In order to make the alignment less critical, mirror M2 will be replaced with a corner-cube retroreflector.

Fig. 3. Picture of the optical board and the mirrors for the stability and noise test. The two white fibers are the input radiations from the laser source; the two yellow fibers are the output radiation towards the detectors.

IV. CHARACTERIZATION OF THE INTERFEROMETER RESOLUTION

The typical errors sources (uncertainty) of a heterodyne interferometer are the random noise (due to the opto-mechanic instability, to the frequency stability of the laser source and to the electronic noise of the detectors and the phase meter) and the cyclic error due to cross-talk between optical signals. In this section we present and discuss the random noise and in the next we will present and discuss the cyclic errors.

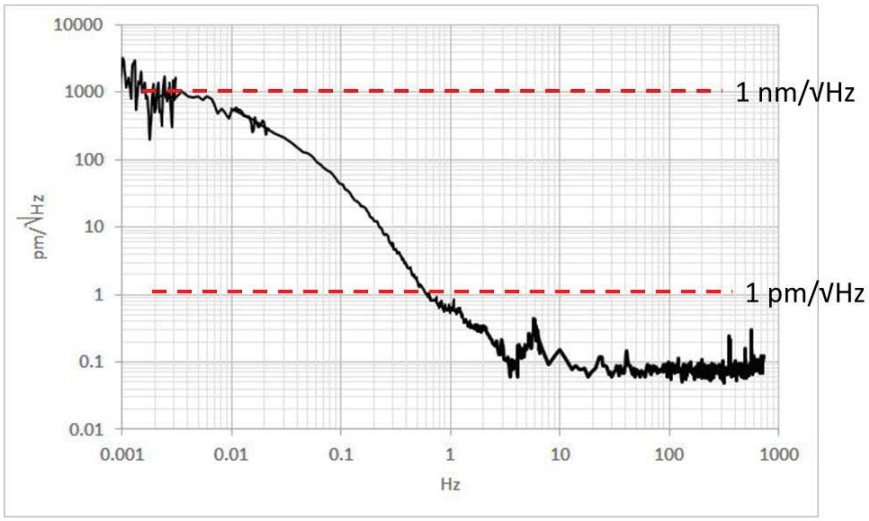

Fig. 4. Power spectral density of the interferometer output when the mirrors are fixed. The residual noise is a limit for the measurement. The two curves are taken with the interferometer balanced (blue) and with 15 mm unbalance (red). The noise is due to laser instability combined to the unbalance of the interferometer, the electronics noise, the acousto-mechanical noise of the environment and the thermo-mechanical drift of the optical components.

The preliminary results presented in Fig. 4 represent the typical spectral noise density of the interferometer when the interferometer is unbalanced by few millimeters. The spectral noise density of the balanced interferometer gives the same values, meaning that the laser frequency noise is not a limit as is explained later in this section. That spectral density includes all noise sources quoted above excluded the cyclic errors. In particular it can be observed that at high frequencies (where the noise is limited by the electronics and shot noise) the noise level is around 0.1 pm/√Hz, while at low frequency the noise is increasing up to the level of 1 nm/√Hz at 0.001 Hz. At low frequencies, there are two predominant phenomena: the first is the effect of the laser frequency stability in combination with the unbalance of the interferometer, the second is due to thermo-mechanical drifts of the components of the interferometer and effects due to the polarization rotation in the fibers. The frequency fluctuations of the laser, indeed, couples with the difference in length of the two arms of the interferometer generating a fluctuation in phase, which is seen as displacement noise. In practical system this effect can be reduced by reducing the unbalance of the interferometer arms or, when this is not possible, by stabilizing the frequency of the laser against some molecular reference or some ultra-stable Fabry-Perot cavity. Both stabilization techniques are rather complex and would significantly increase the size of the interferometer, therefore we chose to use the non-stabilized free running laser described in section III. We have measured the frequency fluctuations of the laser and we have estimated the effect on the displacement noise as a function of the unbalance of the arms of the interferometer. The results are presented in Fig. 5. On the same picture we report the readout noise of capacitive sensors in accelerometers for space mission as reported in [1-3] for comparison. Finally, we have added the approximate curve obtained from the experimental results as reported in Fig. 4. At low frequencies, the noise we have observed is higher (also for zero unbalance) than the simulation results. This demonstrate that at present we are not limited by the laser stability, but rather by noise due to unwanted random polarization rotation occurring in the fibers from the laser source to the interferometer. Indeed, by applying slow mechanical vibrations and temperature variations to the fiber patch cords we have verified an induced effect on the displacement time series. We expect that the low frequency noise can be reduced down to the theoretical limit by reducing the length of the fibers and by operating in a more stable and vibration free environment.

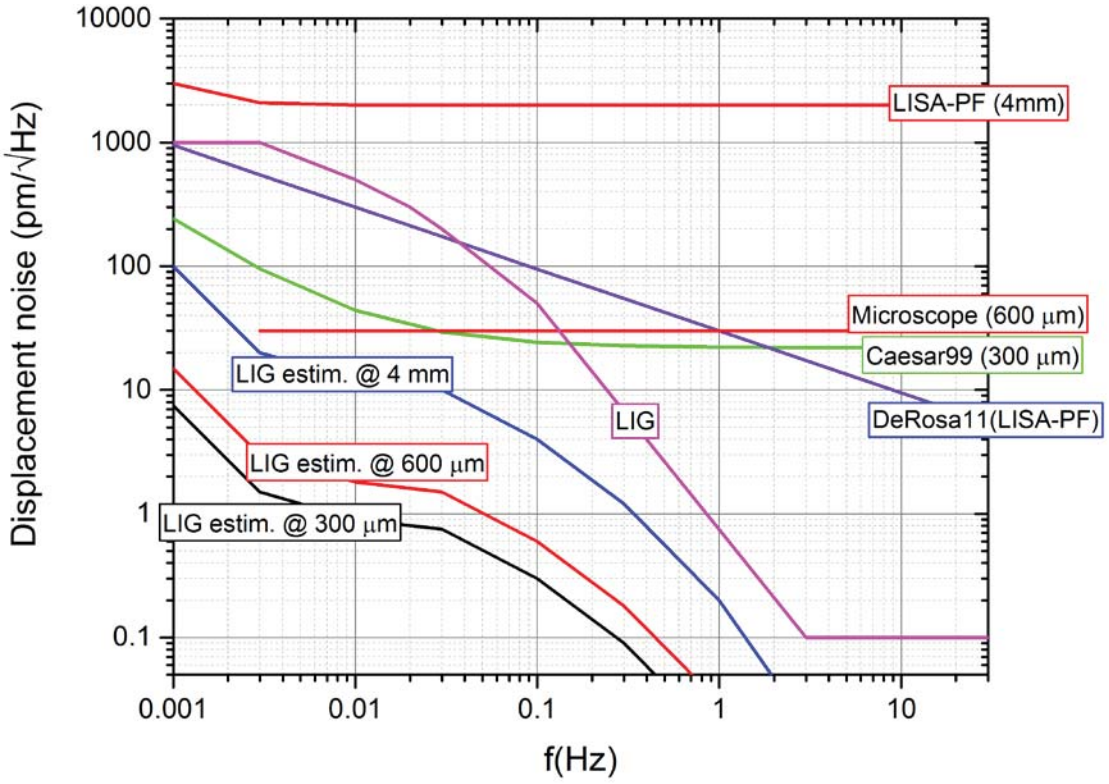

Fig. 5. Comparison between the readout noise of capacitive sensors in accelerometers for space mission as reported in [1-3] and the theoretical noise limit of an interferometric readout. The LIG theoretical limit has been calculated for different arm unbalances equal to the operative working distances of the reported capacitive readouts (black, red and blue curves). We also have reported the approximate curve of the measured LIG noise (magenta curve).

V. Characterization of the Interferometer Non-Linearity

The main systematic error of an interferometric readout is the so-called cyclic error due to the non-ideal behavior of the polarizing optics. A small fraction of the polarized beams runs along the wrong optical path causing spurious interference signals that in turn are sources of non-linearity in the phase-displacement function. The only way to characterize these errors is to compare the reading of the interferometer with an actuator with smaller errors.

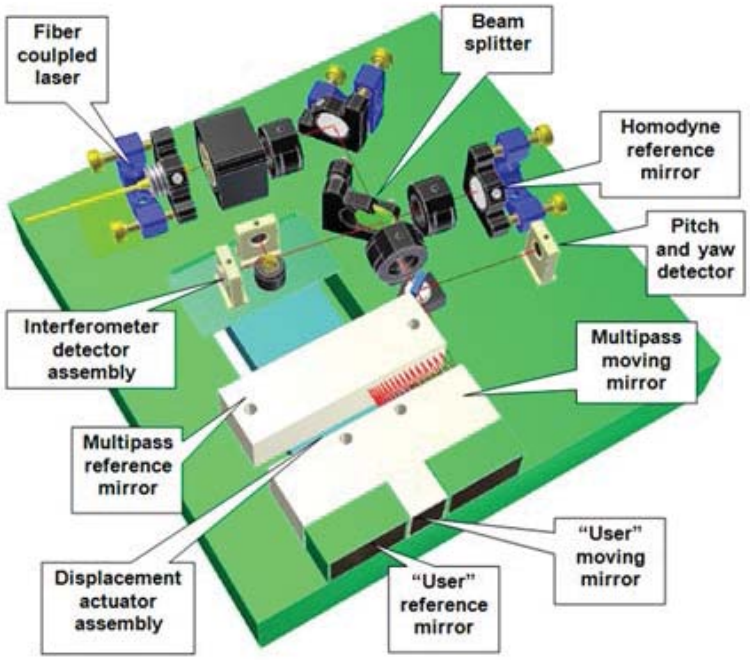

Fig. 6. Rendering of the PRA main components: the actuator relyes on a multiple reflection interferometer as a traceable measurement of the mirror displacement.

We have characterized the LIG by means of a Picometer Reference Actuator (PRA) built to the purpose. The device is described in [11]. It consists in an extremely accurate displacement actuator capable of 100 µm range with subnanometer accuracy, picometer resolution, and submicroradian tip-tilt pointing control, cfr. Fig. 6. The PRA relies on an integrated multiple reflection homodyne interferometer as a high resolution and accurate internal reference, on a multiple reflection based angle sensor, for the active control of the movement straightness, and on a versatile mirrors configuration to transfer the metrological traceability to an external device. The interferometer under test aims at one of the moving mirrors of the PRA and its output is compared with the output of the PRA. The difference between the two readings sets an upper limit to the errors of the interferometer, both in terms of resolution and in terms of non-linearity.

In Fig. 7 is shown a picture of the LIG placed in front of the PRA for the characterization of the first. Mirrors M1 and M2 of Fig. 3 are replaced by two mirrors that fold the two measuring beams towards the mirrors of the PRA.

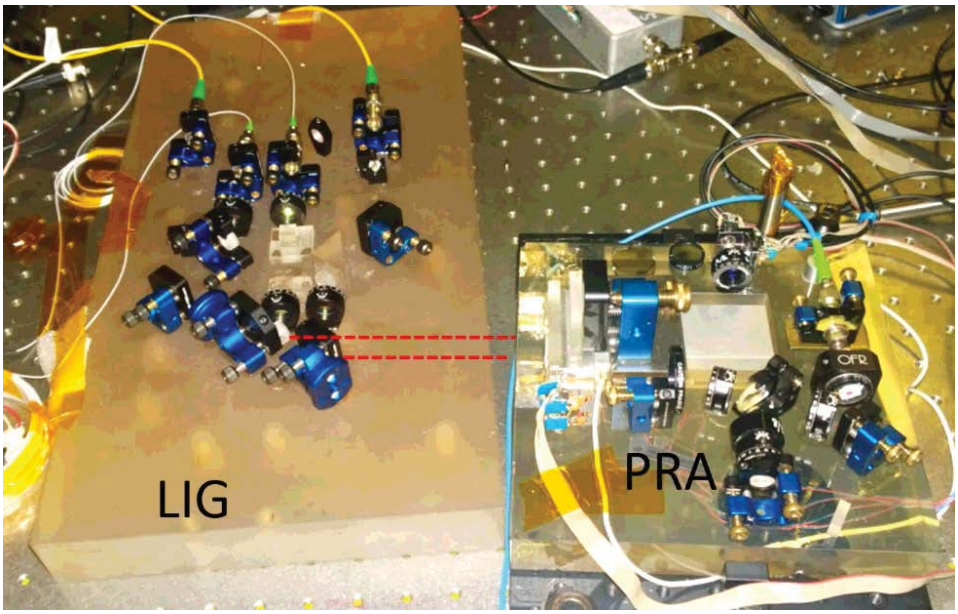

Fig. 7. Picture of the LIG (left) facing the PRA (right) for the characterization of the first. The two beams of the interferometer are folded by means of two mirrors to aim at the fixed and the moving mirrors of the PRA (the path is indicated with dashed red lines).

The following procedure has been implemented: the PRA mirror is moved with a triangular driving signal corresponding to a peak-to-peak displacement of 1500 nm with a frequency of about 1 Hz. The output of the PRA phasemeter and of the LIG phasemeter are recorded and subtracted numerically. The result signal is the combination of the errors of the two interferometers. Since the error of the PRA is less than 50 pm with a periodicity of about 3.5 nm the errors of the two instruments are easily distinguishable. The periodicity of the cyclic errors of the LIG heterodyne interferometer is equal to $\lambda/2 \approx 532$ nm. In Fig. 8 we present a typical result of this comparison with different scans superposed. The single scan represent the error signal with a quasi-sinusoidal function having the expected periodicity of 532 nm and a peak-to-peak amplitude of about 2 nm. The magnitude of this error is typical of a good quality classical heterodyne interferometer caused by 0.2 % polarization mixing. This small periodical errors could be neglected, nevertheless in high resolution applications, if the distortion was not acceptable, the cyclic error can be recorded, mapped and cancelled by post processing.

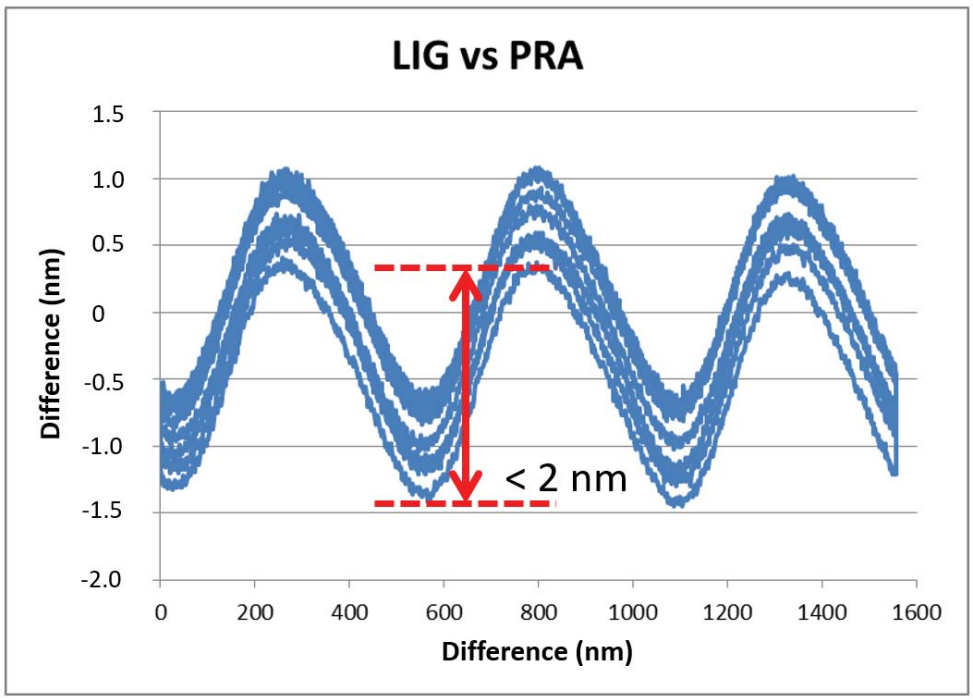

Fig. 8. Characterization of a double beam heterodyne interferometer with the PRA. The PRA mirror is displaced with a triangular movement peak-to-peak displacement of 1550 while the PRA reference interferometer and the LIG interferometer under test are recorded. The non linearity of the latter is given by the difference of the two readings. Several superimposed curves are due to repeated measurements.

VI. The Test Mass and Accelerometer Calibration

The test mass is an aluminum block connected to the frame of the accelerometer through a thin aluminum elastic hinge machined from the same block. The accelerometer was designed to work in absence of gravity, but when operating on the Earth it behaves as an inverted pendulum. Its natural resonance frequency is around 3 Hz depending also from the polarization voltage applied to the driving electrodes. In order to guarantee a stable alignment of the interferometer we foresee to integrate in the test mass a small (5 mm diameter) corner cube reflector, cfr. Fig. 9. A similar reflector will be fixed to the cage of the accelerometer. The practical implementation is described in section VIII. Even if the interferometer guarantees an "absolute" measurement of the displacement of the test mass, we cannot know a priori the sensitivity S of the accelerometer, i.e. the conversion from displacement to acceleration, since it depends on the mechanical properties of the mass spring system. Therefore an accurate calibration is needed.

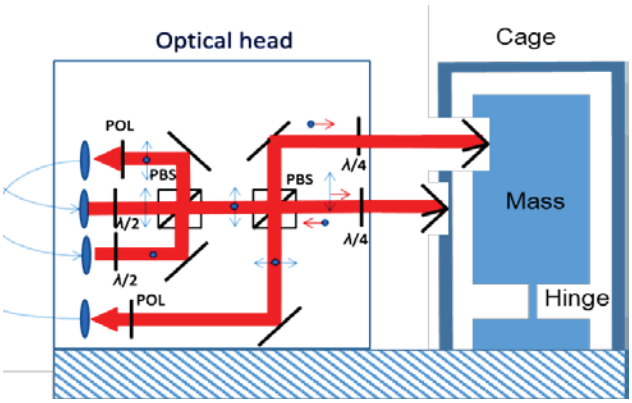

Fig. 9. Scheme of the interferometric readout system coupled with the accelerometer test mass.

We will perform the calibration of the complete instrument with the use of the same facility used for the ISA accelerometers mounted onboard BepiColombo satellite used to measure the gravity field around Mercury. The facility consists of a piezo driven sine-bar nano-angle generator (NAG) which generates a fixed amplitude periodical angular modulation (e.g. 10 μrad p.p. sine modulation at 0.1 Hz). The accelerometer is mounted vertically on the NAG (see Fig. 10) so that the horizontal component of the Earth's gravity field g is the calibrated acceleration acting on the test mass (an angular tilt α with respect to the vertical alignment will generate an acceleration on the horizontal axis $a_{HOR} = g \sin \alpha$). A calibrated autocollimator aiming to a reference mirror fixed to the NAG measures the angles which are recorded together with the accelerometer output by the acquisition system. A Fourier based algorithm will eventually find the calibration constant which ties the interferometer reading with the acceleration. In fact, the calibration process serves to calibrate the force exerted by the electrostatic actuators -embedded in the accelerometer described in section II- on the test mass. This allows to use the force actuator to calibrate the accelerometer once in orbit. Indeed, because of the stresses occurring at the take-off, the mechanical properties of the elastic hinges could change in an unknown way. The calibration strategy and the complete calibration process is described in detail in [12].

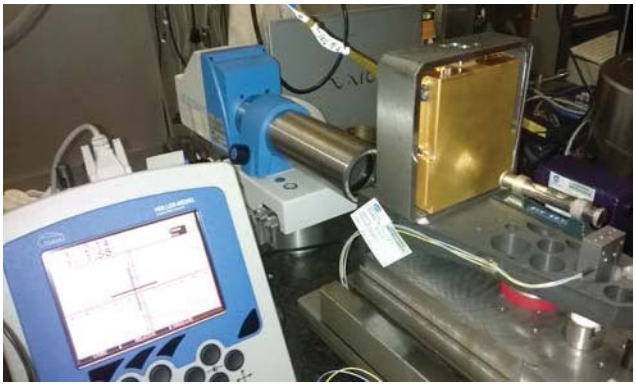

Fig. 10. Calibration of the accelerometer with the sine-bar nano angle generator (NAG). At the right side the nano angle generator with, on top of it, an accelerometer under test (golden box). In the background the autocollimator (AC) aiming at a mirror fixed to the NAG. Left front: the display of the AC.

VII. Evaluation of the Accelerometer Performances

Here we evaluate the theoretical performance of an accelerometer made with a mass-spring system as the one described in [6] equipped with the interferometer described so far for the displacement measurement. We simplify the measured spectral displacement noise (black curve) with the linearized yellow dashed line in Fig. 11. The spectral acceleration noise $S_a(f)$ is related to the experimental spectral displacement noise $S_x(f)$ shown in Fig. 4 with the formula $S_a(f)= S_x(f)/S(f)$. We have assumed a constant noise of 1 nm/√Hz from 1 mHz up to 0.02 Hz, an electronic limited white noise for frequencies above 4 Hz equal to 0.1 pm/√Hz and a constant slope region connecting the two from 0.02 Hz to 4 Hz. We have assumed a resonance frequency $\omega_0 \approx 18.8$ rad/s ($f \approx$ 3 Hz). This leads to the $S_a(f)$ curve shown in Fig. 12 as a solid red line for frequencies from 1 mHz to 1 kHz. Note that we can reduce the resonant frequency of the test mass by means of the electrodes of the accelerometer. When polarized with a constant voltage, they exert an attractive force, which has the effect of a negative spring thus reducing the constant k of the elastic hinge. If we reduce for example the resonant frequency from 3 Hz to 2 Hz, we would improve the low frequency performances of the accelerometer as shown with a dashed red line in Fig. 12.

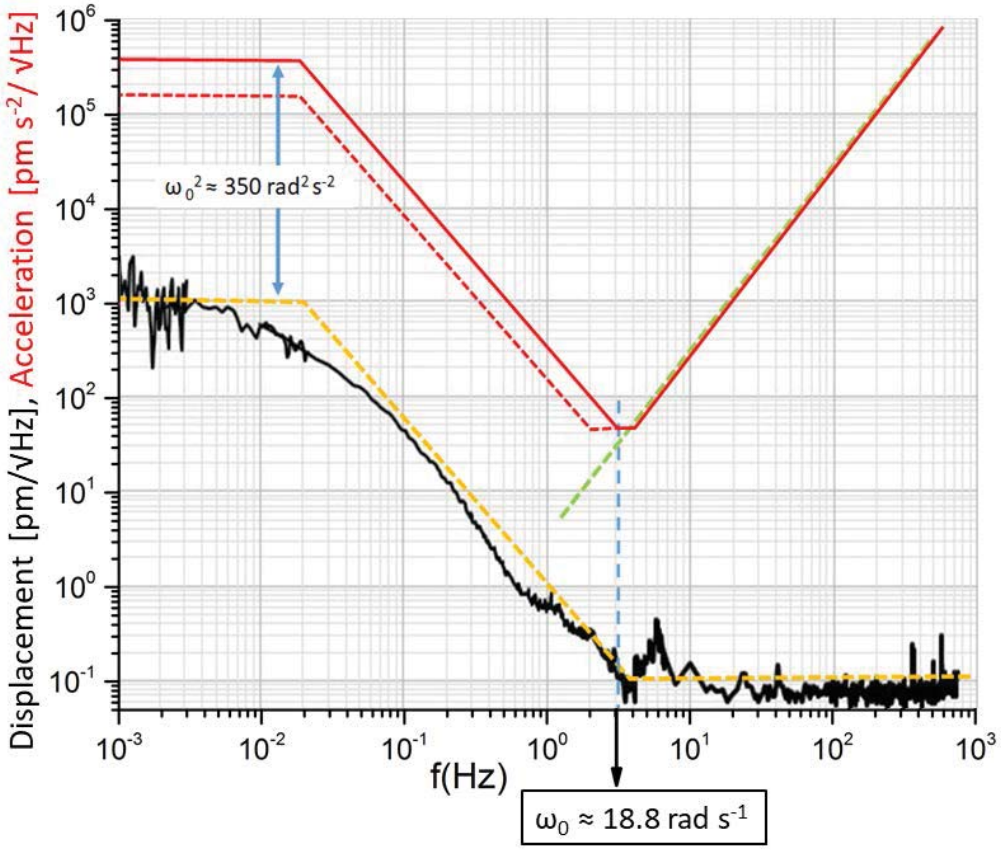

Fig. 11. Expected performance of the accelerometer considering the test mass of ref [6] in combination with the performance of the interferometer as shown in Fig. 4. The black line is interferometer displacement noise $S_x(f)$. The yellow dashed line is the simplified displacement noise $S_x(f)$. The solid red line is the noise $S_a(f)$. calculated considering the natural resonance frequency of the mass spring system f_0 = 3 Hz. The dashed red is calculated for a resonance frequency f_0 = 2 Hz being lowered by applying a constant voltage to the actuators plates of the accelerometer. This performance is conservative since it includes thermo-mechnical drifts which are expected to be lower in space with respect to the laboratory environment.

VIII. LAYOUT OF THE ACCELEROMETER

In Fig. 12 we present a rendering of the accelerometer equipped with the interferometric readout. The interferometer is made with the same components used in the prototype, but mounted in a compact layout to minimize size and weight and to improve the stability. In the proposed solution the interferometer will be fixed directly to the frame of the accelerometer and will measure the displacement between the same and the test mass. A reflector, preferably, a 10 mm corner cube reflector will be embedded in the test mass.

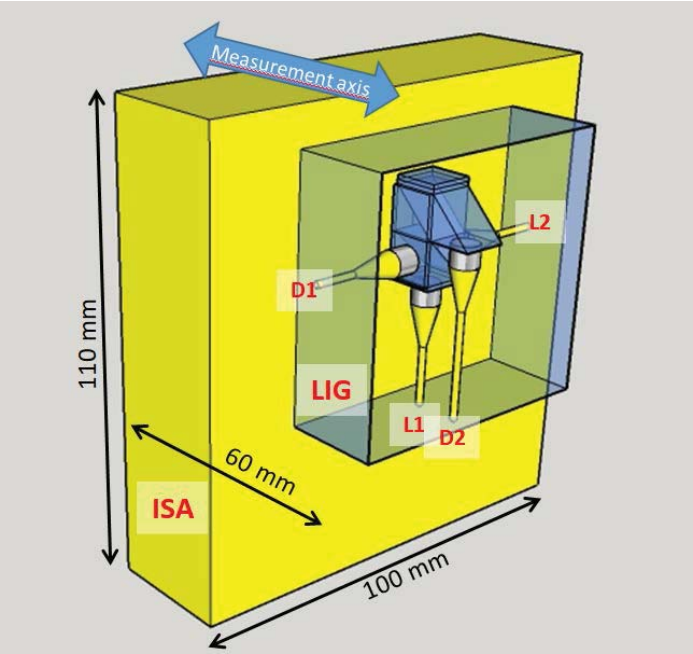

Fig. 12. Rendering of the proposed layout of the accelerometer equipped with the interferometer. The optical components of the interferometer are the same used in the prototype. The yellow block is the ISA accelerometer's cage hiding the test mass. The blue box surrounds the LIG interferometer. L1 and L2 indicate the fibers coming from the laser source, D1 and D2 indicate the fibers going towards the detectors.

The expected final weight of the LIG optical head is less than 100 g excluded the optoelectronic board fiber connected and placed remotely. The last has been estimated to be less than 1000 g. The dimension of the whole accelerometer is contained in a volume of $11\times10\times6$ cm^3.

IX. Conclusions

We propose the use of an interferometric system to measure the displacement of the test mass of an interferometer as a replacement of the classical capacitive readout. To the purpose we have realized a compact all-fiber based heterodyne interferometer (called LIG) to be used onboard space missions where high resolution displacement measurements are required. The interferometer has a resolution of less than 1 pm/√Hz at 1 Hz demonstrating to be competitive with capacitive sensors. The main expected advantage of the interferometer is an increased resolution and the possibility of larger operative distances between the mass and the cage. Furthermore, we have developed the facilities needed to characterize the performances of the interferometer and to calibrate the accelerometer. Finally, the interferometer developed in this work goes in the direction of the realization of an laser interferometer gauge for the measurement of the test masses of the Galileo Galilei (GG) mission [13] requiring a noise floor of 1 pm/√Hz at 1 Hz. Next steps will be the realization of the compact interferometer for the integration in the accelerometer and the reduction of the low frequency noise by the reduction of the optical fiber length.

Aknowledgments

The present work has been partially funded by ESA contract ITI 4000116275/16/NL/MH/GM "LIG, Laser Interferometry Gauge".

References

[1] R. De Rosa, L. Di Fiorea, F. Garufia, A. Gradoa, A. La Rana, L. Milano "An optical readout system for the drag free control of the LISA spacecraft" in Astroparticle Physics Volume 34, Issue 6, January 2011, Pages 394–400

[2] V. Josselin, P. Touboul, R. Kielbasa, “Capacitive detection scheme for space accelerometers applications” in Sensors and Actuators 78, 92-98 (1999)
[3] D. Hudson, R. Chhun, P. Touboul, R. Nicole, “Development status of the differential accelerometer for the MICROSCOPE mission” in Advances in Space Research 39 (2007) 307–314.
[4] M. Pisani et al., "Comparison of the performance of the next generation of optical interferometers", Metrologia 49 455 (2012)
[5] M. Shao, "SIM: the space interferometry mission", Proc. SPIE 3350, Astronomical Interferometry, 536 (1998)
[6] Fuligni F, Iafolla V. Measurement of small forces in the physics of gravitation and geophysics. Il Nuovo Cimento. 1997; 20C(5):619–28
[7] Robertson D I, Fitzsimons E D, Killow C J, Perreur-Lloyd M, Ward H, Bryant J, Cruise A M, Dixon G, Hoyland D, Smith D and Bogenstahl J 2013 “*Construction and testing of the optical bench for LISA Pathfinder*” Classical and Quantum Gravity 30 ISBN: 0264-9381 ISSN
[8] G. Heinzel, B. Sheard, N. Brause, K. Danzmann, M. Dehne, O. Gerberding, C. Mahrdt, V. Müller, D. Schütze, G. Stede, W. Klipsteiny, W. Folknery, R. Speroy, K. Nicklausz, P. Gathx, and D. Shaddock, “Laser ranging interferometer for GRACE follow-on,” in Proceedings of the International Conference on Space Optics, Ajaccio, Corse, France, 2012 (the Centre National d’Etudes Spatiales (CNES), 2012), p. 062.
[9] K. Numata et al. ('Performance of planar-waveguide external cavity laser for precision measurements', Opt. Express 18, 22781-22788 (2010)),
[10] private communication
[11] M. Pisani, A. Giugni, N. Bancone, “A 100 µm range linear actuator with picometer resolution, subnanometer accuracy and submicroradian tip-tilt error for the characterization of measuring instruments at the nanoscale” Proceedings of the 17th international conference Euspen 2017
[12] M. Pisani, M. Astrua, V. Iafolla, F. Santoli, D. Lucchesi, C. Lefevre, M. Lucente “On-ground actuator calibration for ISA-BepiColombo” 2015 IEEE Metrology for Aerospace (MetroAeroSpace)
[13] A.M. Nobili et al., “A.M. Nobili et al., Class. Quantum Grav. 29, 184011 (2012)” in Class. Quantum Grav. 29, 184011 (2012).